

# Multiparticle Collision Dynamics Simulations of the Flagellar Apparatus in *Chlamydomonas reinhardtii*

Sai Venkata Ramana Ambadipudi, Azam Gholami\*

New York University Abu Dhabi, Abu Dhabi, United Arab Emirates

\*azam.gholami@nyu.edu

## Abstract

We investigate the swimming dynamics, orientational behavior, and hydrodynamic interactions of the flagellar apparatus (*FA*) of *Chlamydomonas reinhardtii* using multiparticle collision dynamics (MPCD) simulations. Extending the model established in Yang et al.<sup>1</sup>, we simulate the *FA* as a chain of monomers connected by elastic springs. Our simulations reveal that an *FA* with a nonzero mean curvature in its flagellar beat pattern exhibits sustained ballistic motion for several hundred beats before crossing over to a diffusion-dominated regime due to rotational diffusion. In contrast, *FA*<sub>0</sub>, a flagellar apparatus consisting of two flagella with zero average curvature positioned head-to-head, fails to achieve net propulsion due to its mirror-symmetric deformations, confirming that non-reciprocal shape deformation is necessary but not sufficient condition for propulsion. The orientational auto-correlation function (OACF) of *FA* decays exponentially, aligning with that of an inactive *FA*, while the OACF of *FA*<sub>0</sub> also follows an exponential decay, similar to an inactive *FA*<sub>0</sub>. These findings indicate that active beating does not influence the rotational diffusion of the flagellar apparatus. Additionally, simulations of an asymmetric *FA*, where the arms beat at different frequencies, corroborate experimental observations, revealing a helical swimming trajectory. When two *FAs* swim along the same axis in close proximity, they form stable pairs, leading to enhanced swimming speeds. Conversely, head-on encounters result in mutual blocking, preventing any net displacement. These findings provide valuable insights into the collective behavior of microswimmers and their hydrodynamic interactions in low Reynolds number environments.

## 1 Introduction

Cilia and flagella are slender, whip-like appendages which protrude from the surface of many eukaryotic cells<sup>2,3</sup> and generate propulsion through a characteristic beating motion, exploiting anisotropic viscous drag in the low Reynolds number regime<sup>4-7</sup>. Understanding the hydrodynamics of flagella is crucial, as they play a fundamental role in the motility of various microorganisms, including bacteria and sperm cells<sup>8,9</sup>. This knowledge is essential not only for studying biological systems such as sperm motility and bacterial swarming but also for applications in designing artificial microswimmers<sup>10-14</sup>.

The dynamics of a single flagellum have been extensively studied through experiments<sup>15-18</sup> and simulations<sup>19,20</sup>, leading to significant advancements in understanding flagellar propulsion. Theoretical frameworks have successfully explained the mechanics of flagellar motion<sup>7,17,21</sup>, offering insights into the underlying physics. Additionally, studies on collective behavior<sup>22-25</sup>, such as those by Yang et al.<sup>1,26</sup>, have demonstrated that flagella or sperm cells moving in the same direction experience hydrodynamic attraction, synchronize their beating, and form clusters due to fluid-mediated interactions. These findings highlight the crucial role of hydrodynamic interactions in collective motility.

Despite this progress, the dynamics of flagella that are physically connected remain poorly understood. The coupling between flagella, combined with their hydrodynamic interactions, adds significant complexity to these systems. A key question—relevant both to biological motility and artificial microswimmer design—is whether propulsion efficiency increases with the number of flagella attached to a basal body<sup>27-29</sup>. Additionally, studies have explored the optimal placement of flagella on the basal body<sup>30</sup>. Nature provides examples of microswimmers with multiple flagella, such as *Chlamydomonas reinhardtii*, *E. coli*, *Salmonella typhimurium*, and *Rhizobium lupini*<sup>31,32</sup>. Whether these microorganisms evolved multiple flagella to optimize hydrodynamic

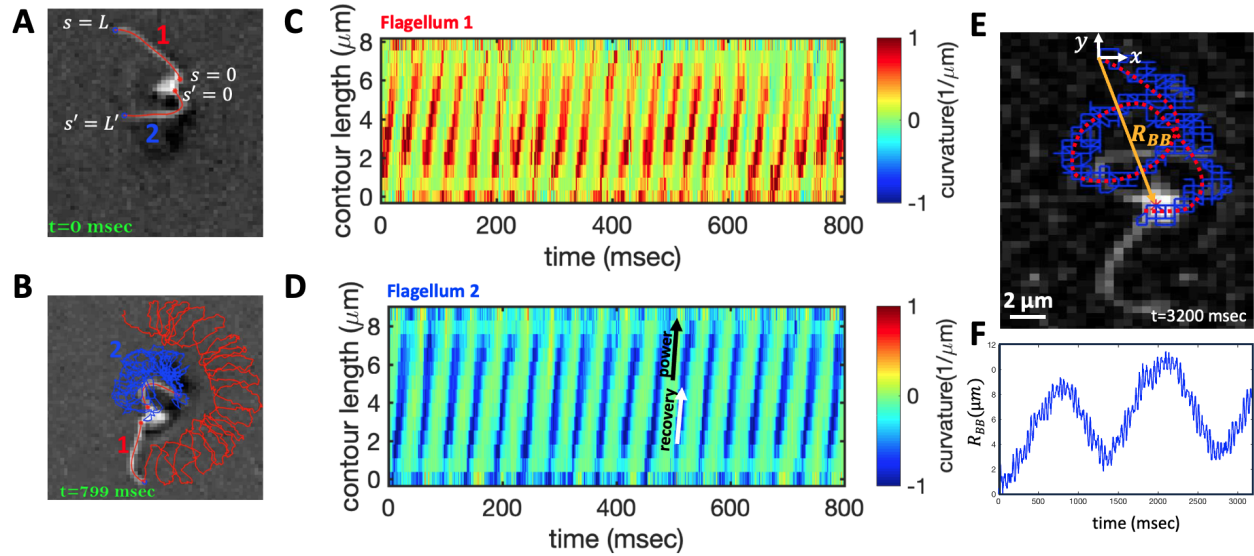


**Figure 1.** A-B) Representative snapshots showing an isolated flagellar apparatus swimming in a water-like fluid supplemented with 2mM ATP. The red and blue trajectories in panel B trace the distal ends of flagella 1 and 2, respectively, as the flagellar apparatus swims. The first flagellum beats at the frequency of 22.50 Hz, while the second one beats faster at frequency of 26.25 Hz. C-D) Propagation of curvature waves along the contour length of both flagella, highlighting the characteristic power and recovery strokes. For each flagellum curvature waves initiate at the basal end at  $(s, s' = 0)$  and propagate toward the distal tip  $(s, s' = L, L')$ . E-F) The geometric center of the basal body, tracked over time, follows a helical trajectory.

interactions remains an open question<sup>33,34</sup>. Furthermore, the role of hydrodynamics in synchronizing flagellar beating when connected to a basal body is yet to be fully understood<sup>35-39</sup>.

*Chlamydomonas reinhardtii*, a single-celled green alga with two flagella protruding from its cell body, serves as an excellent model system for studying the hydrodynamic interactions of physically connected flagella<sup>40,41</sup>. The two flagella of *C. reinhardtii* typically beat in synchrony for extended periods before transitioning to an asynchronous state during re-orientation, after which they regain synchronization<sup>42-44</sup>. While some experiments highlight the significance of hydrodynamic interactions in synchronization<sup>22,45,46</sup>, other experiments with *C. reinhardtii* also support the crucial role of mechanical coupling through basal bodies<sup>36,47-52</sup>. The basal body is composed of elastic fibers with a microtubule-based structure exhibiting periodic striation patterns<sup>48</sup>. In *C. reinhardtii*, these periodic striations are approximately 80 nm apart and have been shown to respond dynamically to chemical stimuli such as calcium ions, indicating the contractile nature of the fibers<sup>53</sup>.

Experiments on the isolated flagellar apparatus (FAs) of a wall-less mutant of *C. reinhardtii*, conducted by Hyams and Borisy<sup>54</sup>, demonstrated that both flagella can sustain their characteristic beating patterns even in the absence of the cell body and cytoplasm. To facilitate microscopy, Hyams and Borisy primarily examined FAs anchored to substrate debris, observing that over 70% exhibited synchronous beating, while the remainder beat asynchronously. They also documented transient switches between synchronous and asynchronous states. More recently, Pozveh et al.<sup>55</sup> investigated freely swimming FAs and found that when the frequency difference between the two flagella was substantial (10 – 41% of the mean), neither mechanical coupling via the basal body nor hydrodynamic interactions were sufficient to achieve synchronization. Despite these insights, experiments with isolated FAs remain challenging due to their low yield, with successful isolation and reactivation of FAs occurring in only a small percentage of attempts. Furthermore, most isolated apparatuses exhibit frequency differences exceeding 15%, making large-scale statistical analysis difficult. Given these limitations, developing a reliable computational model of the FAs is essential to complement experimental findings and enable systematic investigations.

In this study, we build upon the framework introduced by Yang et al.<sup>1</sup> to develop a model for the FAs and employ multiparticle collision dynamics (MPCD) simulations to examine their swimming dynamics. The paper is structured as follows: Section II provides an overview of the experimental observations that motivated this

research. Section III presents the details of our modeling approach and the MPCD methodology. In Section IV, we analyze the swimming dynamics and orientational behavior of a single *FA*, while Section V examines the hydrodynamic interactions between two *FAs*. Finally, Section VI summarizes our key findings and discusses their implications for flagellar collective motility.

## 2 Experimental motivations

In our previously published work<sup>55</sup>, we utilized high-speed imaging, quantitative image processing, and mode analysis to investigate the wave dynamics of the *FAs* isolated from a wall-less strain of *C. reinhardtii*. The isolation procedure followed the protocol established by Hyams and Borisy<sup>54,56</sup>, which yields a low success rate, with only 2–3% of cells releasing their *FAs*. Figure 1A-B presents an example of an isolated *FA* reactivated with 2mM ATP in the buffer (refer to Ref. <sup>55</sup> for experimental details). Upon reactivation, curvature waves initiate from the basal ends, where the two flagella connect to the basal body, and propagate toward the distal tips (Fig. 1C-D). The frequency of these curvature waves varies with ATP concentration, following a Michaelis-Menten-type dependency<sup>57–60</sup>. As the *FA* swims, the basal body follows a helical trajectory, as shown in Fig. 1E-F. The trajectory exhibits a high-frequency oscillatory motion, with a characteristic frequency of approximately 22 Hz, superimposed on larger-scale oscillations occurring at a much lower frequency of around 0.8 Hz.

## 3 Simulation method

In this work, we utilize the multiparticle collision dynamics (MPCD) method<sup>61</sup>, combined with molecular dynamics, to simulate the two-dimensional swimming dynamics of a *FA* in a fluid<sup>1,26</sup>. The MPCD technique is a well-established computational tool that has been widely applied to model the hydrodynamics of active matter and polymeric systems<sup>62–69</sup>. In addition to solving coarse-grained Navier-Stokes equations, MPCD inherently incorporates thermal fluctuations, making it a powerful tool for realistic hydrodynamic simulations. In this framework, fluid dynamics is governed by the MPCD method, while the motion of the *FA* is described using molecular dynamics, ensuring an accurate representation of both hydrodynamic interactions and flagellar movement.

### 3.1 Multi particle collision dynamics for fluid

In the MPCD framework, the fluid is represented by point particles, each labeled by an index  $i$ , with mass  $m^f$ , position  $\mathbf{r}_i^f$ , and velocity  $\mathbf{v}_i^f$ . The fluid system is initialized by distributing these particles within a simulation box of size  $L_{\text{box}} \times L_{\text{box}}$  such that each collision cell of size  $a \times a$  contains, on average,  $\rho \sim 10$  particles, where  $a \ll L_{\text{box}}$ . Let  $\delta t$  be the time step used to update the positions and velocities of the particles. During each  $\delta t$ , the system undergoes two key steps:

1. *Streaming Step*: Particles move ballistically, updating their positions according to:

$$\mathbf{r}_i^f(t + \delta t) = \mathbf{r}_i^f(t) + \mathbf{v}_i^f(t)\delta t. \quad (1)$$

2. *Collision Step*: Particles within each collision cell interact and exchange momentum through stochastic collisions, implemented using the Andersen thermostat<sup>63</sup>. The post-collision velocities are given by:

$$\mathbf{v}_i^f(t + \delta t) = \mathbf{v}_{cm}^f(t) + \mathbf{v}_i^{\text{rand}}(t) - \mathbf{v}^{\text{rand}}(t). \quad (2)$$

The velocities  $\mathbf{v}_i^{\text{rand}}(t)$  are drawn from a normal distribution with variance  $k_B T / m^f$ , ensuring a Maxwell-Boltzmann velocity distribution at equilibrium. The center-of-mass velocity of particles within a given collision cell  $c$  at time  $t$  is defined as:

$$\mathbf{v}_{cm}^f(t) = \frac{\sum_{j \in c} m^f \mathbf{v}_j^f(t)}{\sum_{j \in c} m^f}. \quad (3)$$

Similarly, the mean velocity of the randomly assigned post-collision velocities within the same cell is:

$$\mathbf{v}^{\text{rand}}(t) = \frac{\sum_{j \in c} m^f \mathbf{v}_j^{\text{rand}}(t)}{\sum_{j \in c} m^f}. \quad (4)$$

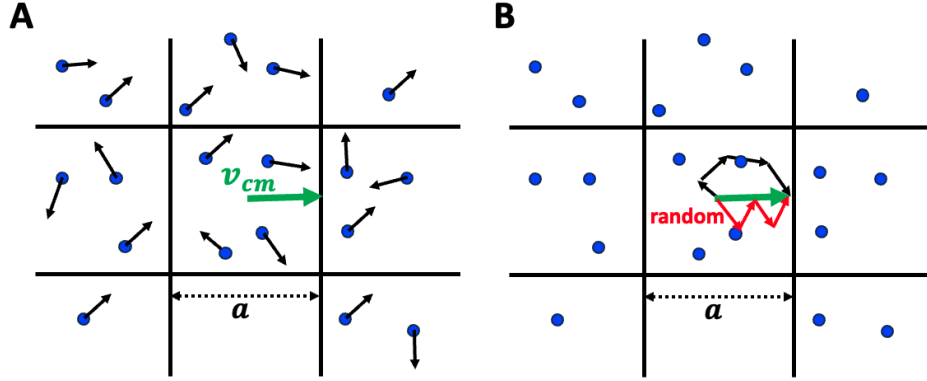


**Figure 2.** Schematic representation of the MPCD framework. (A) The simulation domain is partitioned into square cells of linear size  $a$ . Each particle within a given cell possesses a velocity  $\mathbf{v}_i^f(t)$  (indicated by black arrows). The sum of all particle velocities in cell  $c$  determines the center-of-mass velocity  $\mathbf{v}_{cm}(t)$  (depicted by the green arrow). (B) A stochastic Andersen collision step (see Eqs. 2- 4) is applied within each cell, ensuring momentum conservation. During this step, new random velocities (shown as red arrows) are assigned to the particles in cell  $c$  while maintaining the center-of-mass velocity.

The above collision rule inherently performs thermostating, maintaining a constant temperature by conserving the kinetic energy. It also ensures linear momentum conservation within each collision cell (see Fig. 2). However, angular momentum is not conserved by default. To restore angular momentum conservation, the post-collision velocities in Eq. (2) are modified by applying a rigid-body rotation correction:

$$\begin{aligned} \mathbf{v}_i^f(t + \delta t) = & \mathbf{v}_{cm}^f(t) + \mathbf{v}_i^{rand}(t) - \mathbf{v}^{rand}(t) \\ & + m^f \Pi^{-1} \sum_{j \in c} [\mathbf{r}_j \times (\mathbf{v}_j^{rand} - \mathbf{v}_j^f)] \times \mathbf{r}_i, \end{aligned} \quad (5)$$

where  $\Pi$  is the moment of inertia tensor of the particles in the collision cell.

Additionally, the algorithm must be corrected for Galilean invariance, which is achieved by applying a random grid shift to the entire simulation box before each collision step<sup>70,71</sup>. Specifically, all particles are displaced by a random vector whose components are uniformly distributed in the interval  $[-a/2, a/2]$ . After the collision step, the particles are shifted back by the same magnitude in the opposite direction. This grid shift correction is particularly necessary when the mean free path of the fluid particles is smaller than the collision cell size  $a$ .

### 3.2 Model for Flagellar Apparatus

The flagellar apparatus (*FA*) is modeled as a chain of  $N_b$  monomers, each with mass  $m^b$ , connected by elastic springs, extending the framework established in Ref.<sup>26</sup>. The total energy of the *FA* is given by:

$$\begin{aligned} E = & \sum_{i=1}^{N_b-1} \frac{k}{2l_0^2} (|\vec{R}_i| - l_0)^2 + \sum_{i=1}^{N_b/2} \frac{\kappa}{2l_0^3} (\vec{R}_i - \mathbf{R}^T(l_0 C(s_{i+1}, t)) \vec{R}_{i+1})^2 \\ & + \sum_{i=N_b/2}^{N_b} \frac{\kappa}{2l_0^3} (\vec{R}_{i+1} - \mathbf{R}(l_0 C(s_{i+1}, t)) \vec{R}_i)^2 + V. \end{aligned} \quad (6)$$

The first term represents the harmonic potential arising from the springs connecting the monomer beads, with a spring constant  $k$  and equilibrium bond length  $l_0$ . The summation runs over all beads in the chain, and  $\vec{R}_i$  denotes the bond vector pointing from bead  $i$  to bead  $i + 1$ . The second and third terms account for the bending energy of the *FA*, characterized by the bending rigidity  $\kappa$ . Here,  $\mathbf{R}$  is a two-dimensional rotation operator that rotates a vector clockwise by  $l_0 C(s, t)$ , and  $\mathbf{R}^T$  represents its transpose. The function  $C(s, t)$

describes the curvature along the contour length  $s$  at time  $t$ , defined as:

$$\begin{aligned}
C(s,t) &= C_0 + A \cos \left( 2\pi \left( -\frac{1}{\lambda} \left( s - \frac{(N_b - 1)l_0}{2} \right) - ft + \phi_1 \right) \right) \\
&\times \Theta \left( s - \frac{(N_b - 1)l_0}{2} \right) + A \cos \left( 2\pi \left( \frac{1}{\lambda} \left( s - \frac{(N_b - 1)l_0}{2} \right) - ft + \phi_2 \right) \right) \\
&\times \left( 1 - \Theta \left( s - \frac{(N_b - 1)l_0}{2} \right) \right), \tag{7}
\end{aligned}$$

where  $\Theta$  is the Heaviside step function,  $C_0$  is the mean curvature of the  $FA$ ,  $f$  is the flagellar beat frequency,  $A$  represents the amplitude of the curvature waves, and  $\lambda$  denotes the wavelength of the curvature wave, which is assumed to be the same as the contour length of each flagellum. We also assume that the phase difference between the two flagella is zero, i.e.,  $\phi_1 = \phi_2$ . This equation describes curvature waves that propagate symmetrically from the center toward both ends. The final term in Eq. (6) represents the volume exclusion energy  $V$ , which is incorporated only in simulations of two interacting  $FA$ s. The steric repulsion among the monomers of the two  $FA$ s is enforced using a shifted and truncated Lennard-Jones (LJ) potential. The total potential energy for a system of  $N_b$  particles interacting via this LJ potential is defined as:

$$V = \sum_{i=1}^{N_b^1} \sum_{j=1}^{N_b^2} U(r_{ij}), \tag{8}$$

where indices 1 and 2 denote the first and second  $FA$ , respectively. The pairwise potential  $U(r_{ij})$  is given by:

$$U(r_{ij}) = \begin{cases} 4\epsilon \left[ \left( \frac{\sigma}{r_{ij}} \right)^{12} - \left( \frac{\sigma}{r_{ij}} \right)^6 \right] - U(r_c), & r_{ij} \leq r_c, \\ 0, & r_{ij} > r_c, \end{cases}$$

with the potential at the cutoff distance  $r_c$  defined as:

$$U(r_c) = 4\epsilon \left[ \left( \frac{\sigma}{r_c} \right)^{12} - \left( \frac{\sigma}{r_c} \right)^6 \right].$$

Here,  $r_{ij} = |\mathbf{r}_i - \mathbf{r}_j|$  represents the distance between beads  $i$  and  $j$ , while  $\epsilon$  which is set to be  $660k_B T$  determines the depth of the potential well,  $\sigma = a$  defines the characteristic length scale, and  $r_c = 2^{1/6}a$  is the cutoff distance beyond which the interaction is set to zero.

The curvature waves that pass through the  $FA$  induce a time-dependent bending force, rendering it active. During the streaming step, the beads of the  $FA$  are moved using the velocity-Verlet algorithm with a time step much smaller than the MPCD time step. We choose  $\delta t_b = \delta t/100$ . Thus, during each streaming step of MPCD, while the fluid particles are advanced by one step of  $\delta t$ , the beads are advanced by 100 steps of  $\delta t_b$ . In the collision step, the beads are sorted into the cells along with fluid particles and are considered in the calculation of the velocities as in Eq. (5).

We use the MPCD units for all the quantities in the simulation. The length is measured in units of  $a$ , the cell size. Energy is measured in units of  $k_B T$ . Mass is measured in units of  $m^f$ . In these units, the time unit becomes  $\tau_{\text{MPCD}} = a\sqrt{m^f/k_B T}$ . We employ periodic boundary conditions. The values of the hyperparameters in the method are taken from Ref. <sup>26</sup>. The  $FA$  is chosen to have  $N_b = 101$  beads. The values of key parameters are as follows: Time step  $\delta t$  is taken to be 0.025, size of the simulation box  $L_{\text{box}} \times L_{\text{box}}$  is chosen to be  $200 \times 200$ , equilibrium distance between the springs is taken to be  $l_0 = a/2$ , spring constant is chosen to be  $k = 1.25 \times 10^4 k_B T$ , and bending rigidity is set as  $\kappa = 200k_B T(N_b - 1)l_0$ . These values are chosen so that the persistence length is much larger than the total length of the  $FA$ , given by  $L = 100l_0$ , and the structure of the  $FA$  remains stable, withstanding thermal fluctuations. The mass of each bead of the  $FA$  is taken to be  $m^b = 10m^f$ . The frequency  $f$  of the curvature wave is chosen such that  $f^{-1} = T_b = 120 \tau_{\text{MPCD}}$ , where  $T_b$  represents the flagellum beat period. The amplitude of the curvature wave is set to  $A = 0.2$ , and the mean curvature is taken to be  $C_0 = 0.1$  (both in units of  $a^{-1}$ ). With the chosen parameters, we estimate the Reynolds number to be  $O(10^{-2})$ <sup>26</sup>, ensuring that the simulation accurately represents the low-Reynolds-number environment experienced by microorganisms.

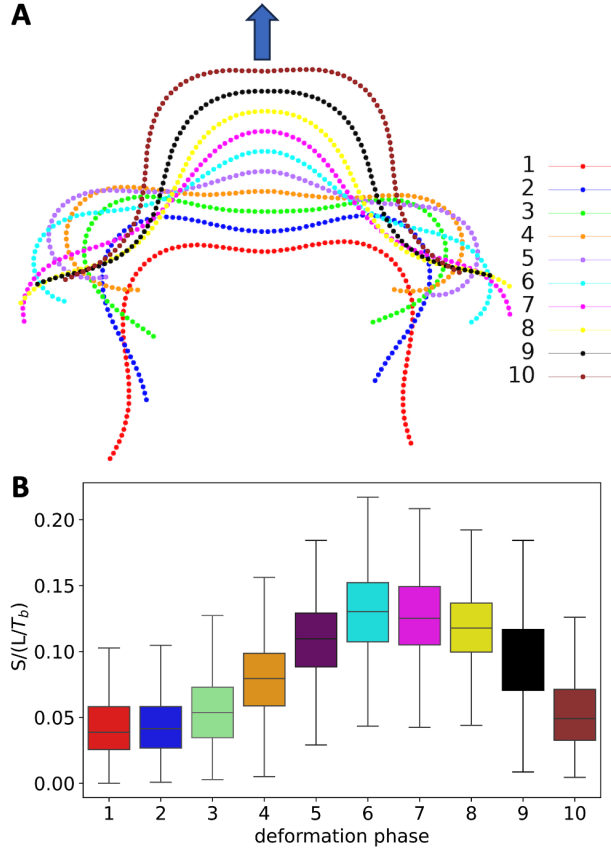


**Figure 3.** (A) Equidistant phases of the *FA* within a beat cycle. A complete sine-like wave propagates through each arm as the *FA* transitions from phase 1 to phase 10. Successive phases are displaced in the direction of motion of the *FA*. The arrow indicates the direction of motion for visual reference. (B) Speeds corresponding to the beat phases of the *FA*. Phases 4 to 8 constitute the power stroke, while the remaining phases belong to the recovery stroke; see also Video 1.

## 4 Hydrodynamics of a single flagellar apparatus

Using the selected hyperparameters and the methodology detailed in Section III, we conducted MPCD simulations of a *FA* swimming in a fluid. Simulations were conducted for three distinct cases: a flagellar apparatus with a nonzero average curvature  $C_0$ , which we denote as *FA*; a flagellar apparatus with zero average curvature, referred to as *FA*<sub>0</sub>; and their corresponding inactive counterparts, *FA*<sub>i</sub> and *FA*<sub>i0</sub>, respectively, for comparison. The inactive cases were simulated by setting the curvature wave frequency  $f$  in Eq. (7) to zero. In this section, we analyze the simulation results and compute key properties to examine the dynamical behavior of the *FAs*.

### 4.1 Flagellar apparatus with non-zero mean curvature (*FA*)

Figure 3A illustrates a sequence of equidistant phases of the *FA* within a beat cycle. The beating motion arises due to the traveling curvature waves incorporated into the Hamiltonian of the *FA*; see Eqs. (6)-(7). The effective curvature of the *FA* is a result of its interaction with the surrounding fluid. As shown in Fig. 4, the resultant curvature wave along the *FA*'s contour closely resembles the input curvature wave. These two sinusoidal-like traveling waves, originating from the center of the *FA* and propagating in opposite directions along its contour, drive the forward motion of the *FA*, as depicted in Fig. 3.

The speeds corresponding to each phase in the sequence of the *FA*'s beat cycle are presented in Fig. 3B. Each phase exhibits a speed distribution, with the average speed over a complete beat cycle being approximately 0.09 (in units of  $L/T_b$ ). It is evident that the average speeds during phases 4 to 8 are higher compared to the other phases, with peak speeds reaching approximately 0.18 during phases 6 and 7. These phases correspond

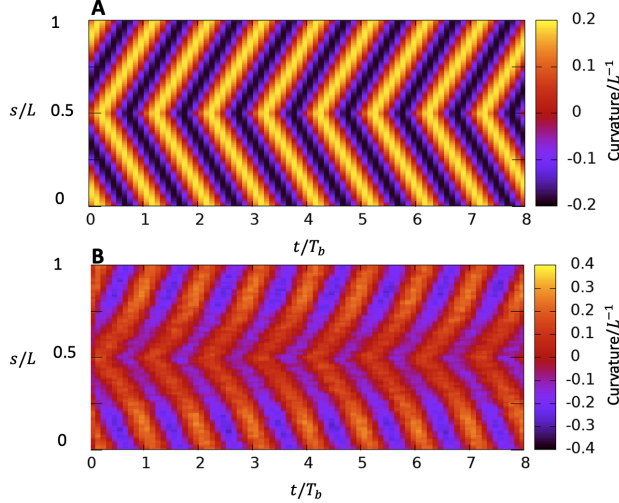


**Figure 4.** (A) Input curvature wave along the *FA* as defined in Eq. (7). (B) Resultant curvature wave along the *FA*, obtained from simulation data. The resultant curvature wave closely follows the input curvature wave.

to the power stroke of the *FA*. In contrast, phases 9, 10, and 1 to 3 represent the recovery stroke, during which the speeds are relatively lower than those observed in the power stroke.

Flow fields corresponding to phases 1 and 2, which are part of the recovery stroke, are depicted in Fig. 5. Note that all the flow fields presented in this study are shown in a body-fixed frame, where the frame is attached to the central bead of the *FA*, with the tangent at the central bead aligned along the  $x$ -axis. The flow fields displayed here represent the resultant fluid velocity in the body-fixed frame, after subtracting the constant field of the average velocity of the fluid in this frame<sup>72</sup>. During phases 1 and 2, the *FA* experiences an incoming flow along its direction of motion, as illustrated in Fig. 5. In contrast, flow fields for phases 6 and 8, which belong to the power stroke, are shown in Fig. 6. During these phases, the *FA* encounters an outgoing flow along its direction of motion. Across all phases, the fluid along each arm of the *FA* contains two vortices of opposite polarity. As the arms beat, these vortices travel from the center of the *FA* toward the ends, mimicking the behavior of a single flagellum<sup>72</sup>. The beat-averaged flow field of the *FA* is presented in Fig. 7. To classify the *FA* within a known swimmer category, we attempted to determine its far-field flow structure by coarse-graining the flow field over larger cell sizes. However, our efforts were unsuccessful, as no distinct far-field pattern emerged. One possible reason for this is the periodic boundary conditions, which constrain correlations to the size of the simulation box. Additionally, thermal fluctuations contribute to the disruption of long-range correlations.

We compared the beat-averaged flow field in Fig. 7 with that computed in Ref.<sup>73</sup>, where the Navier–Stokes equation was solved using experimentally measured flagella shapes for *C. reinhardtii*. The beat-averaged flow field of the *FA* closely matches the beat-averaged flow field reported in Ref.<sup>73</sup>. Furthermore, the flow field of the *FA* is also similar to the experimentally measured flow field of *C. reinhardtii* in Ref.<sup>41</sup>. From these observations, we conclude that the *FA* likewise swims as a puller.

## 4.2 Flagellar apparatus with zero mean curvature ( $FA_0$ )

It is well known that at low Reynolds numbers, successful swimmers must exhibit non-reciprocal body kinematics. In his seminal paper, Purcell<sup>4</sup> formulated the so-called *Scallop theorem*, which states that if the sequence of shapes adopted by a swimmer undergoing time-periodic deformations remains identical after a time-reversal transformation, then the swimmer cannot achieve net displacement. Mathematically, non-reciprocal kinematics is a necessary but not sufficient condition for propulsion<sup>6</sup>. A simple counterexample is a system consisting of two flagella, each with zero mean curvature, that are mirror images of each other and positioned head-to-head ( $FA_0$ ). Although their combined motion is non-reciprocal, the mirror symmetry of the system prevents any net displacement of the center of mass, effectively canceling out any propulsion. Below, we present our MPCD simulation results for  $FA_0$ , obtained using the same procedure and parameters as for *FA*, except that  $C_0$  is set to zero.

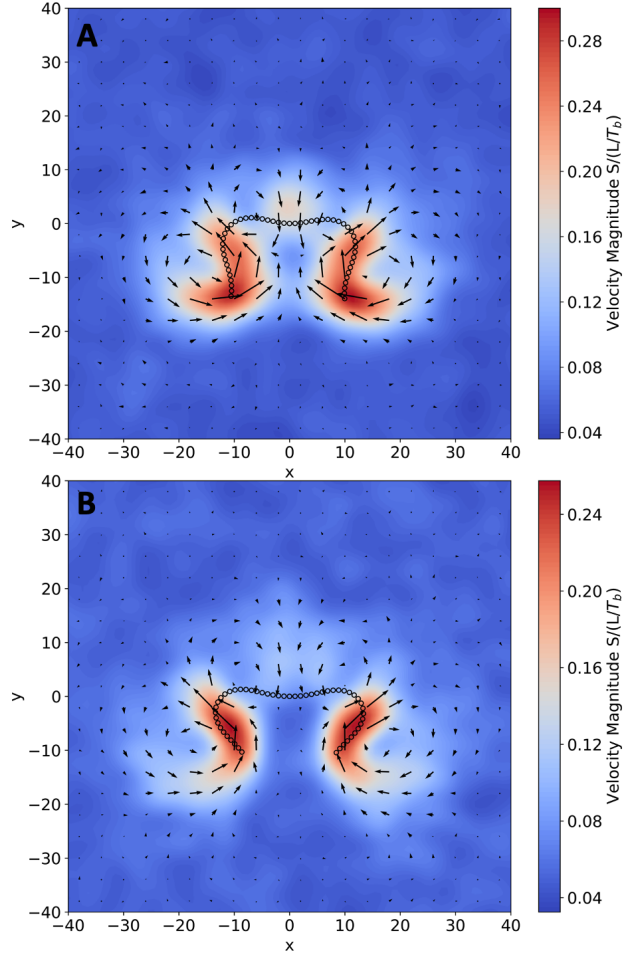


**Figure 5.** Flow fields of phase 1 (A) and phase 2 (B) of the  $FA$  during the recovery stroke. In both phases, the flow field along the axis of motion is directed opposite to the motion of the  $FA$ . Notably, the magnitude of the flow field along the direction of motion is relatively smaller than the peak values, which occur at the ends of the arms.

Figure 8 illustrates the various phases of  $FA_0$  during a beat cycle. Notably, the first five phases are mirror images of the subsequent five phases, respectively. However, the mirror symmetry is slightly disrupted due to thermal fluctuations. Similar to the case of  $FA$ , the resultant curvature wave of  $FA_0$  closely resembles the input curvature wave. The speeds corresponding to each phase are plotted in Fig. 8. As in the case of  $FA$ , the speeds of each phase of  $FA_0$  exhibit a distribution, which we attribute to thermal fluctuations. It can be observed from the figure that the speed distributions of corresponding mirror-image phases are nearly identical.

Flow fields around the mirror-symmetric phases 3 and 8 of  $FA_0$ , as obtained from our simulations, are shown in Figure 9. The results indicate that the flow fields corresponding to these phases are also mirror-symmetric, consistent with the symmetry of the phases themselves.

The beat-averaged flow field of  $FA_0$  is presented in Fig. 10. This flow field exhibits mirror symmetry along both the  $x$ - and  $y$ -axes. The beat-averaged flow field of a single flagellum<sup>26</sup> consists of two vortices near its rear end and an inflow perpendicular to its axis close to its head. A similar pattern can be observed in the beat-averaged flow field along each arm of  $FA_0$  in Fig. 10. Thus, the flow field of  $FA_0$  may be interpreted as the net field generated by two flagella connected head-on.

Ideally, the mirror symmetry observed in the computed flow fields and speed distributions implies that the displacement generated during the first five phases should be exactly canceled by the displacement from the subsequent five phases. However, thermal fluctuations introduce variations in the speed of each phase, resulting in a distribution of possible velocities. Consequently, perfect cancellation may not occur, leading to



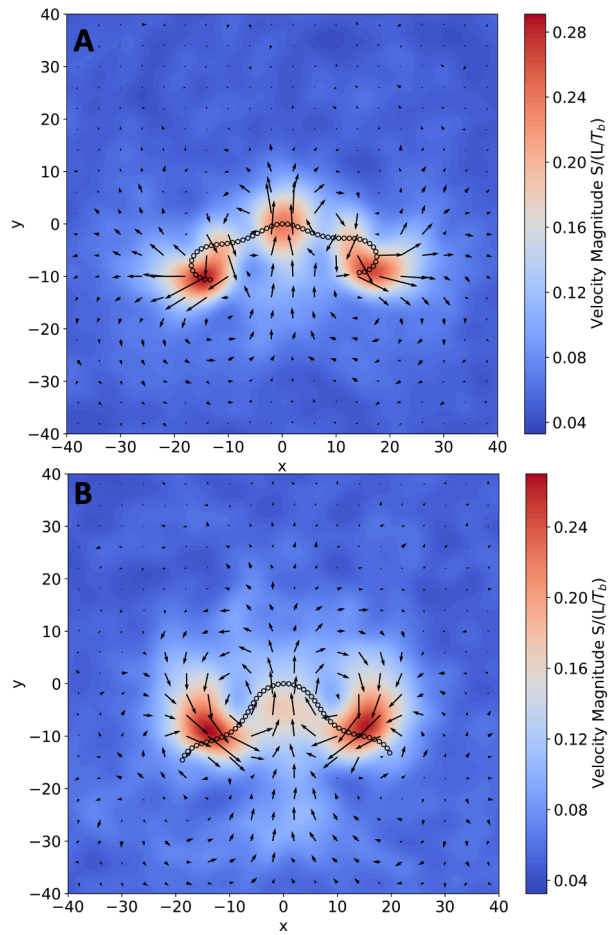


**Figure 6.** Flow fields of phases 6 (A) and 8 (B) of the *FA* during the power stroke. The flow field along the axis of motion is aligned with the direction of motion of the *FA*. The magnitude of the flow field along this direction is close to its peak value.

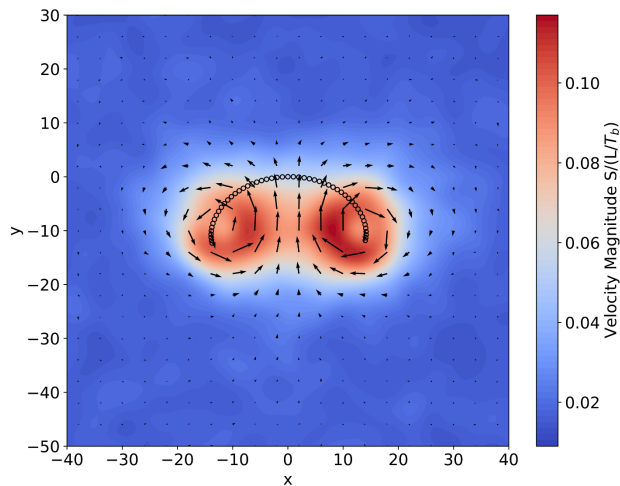


**Figure 7.** Flow field of *FA* averaged over a beat cycle. The flow field along the axis of motion is directed in the same direction as the power stroke. The flow field decays rapidly and leaves no detectable signature beyond distances greater than twice its size.

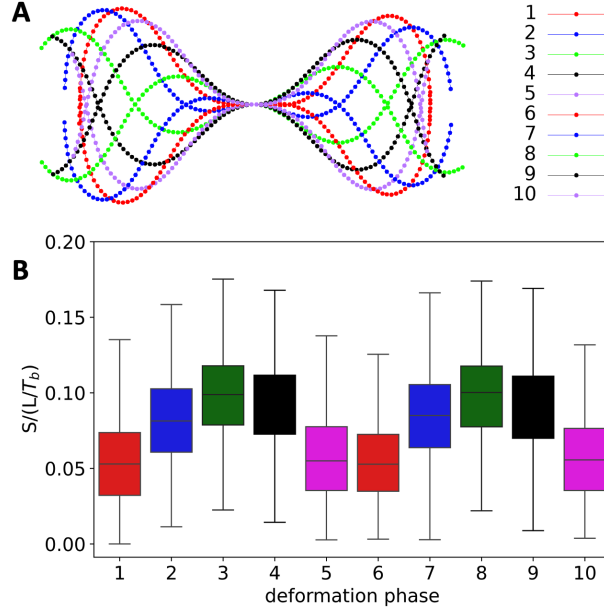


**Figure 8.** (A) Equidistant phases of  $FA_0$ , with mirror images plotted in the same color. (B) Speeds of the phases of  $FA_0$ , where the speed distributions of corresponding mirror-symmetric phases are similar; see also Video 2.

small random displacements. In the next section, we compute the mean square displacement (MSD) and other related quantities to investigate the dynamics of  $FA_0$  in comparison to  $FA$ .

### 4.3 Mean square displacement

The trajectories of  $FA$ ,  $FA_0$ , and  $FA_{i0}$  (inactive  $FA_0$ ) over a time span of 200 beats of  $FA$  are shown in Fig. 11. From the figure, it is evident that  $FA$  exhibits directed swimming, covering a significantly greater distance compared to  $FA_0$  and  $FA_{i0}$ . The  $FA$  predominantly moves in the direction indicated by the arrow in Fig. 3 and follows an approximately straight trajectory before undergoing directional changes due to reorientation, as we demonstrate below. In contrast, the distances covered by  $FA_0$  and  $FA_{i0}$  are of the same order of magnitude, with their motion primarily governed by diffusion, as corroborated by the MSD analysis discussed in the following section.

We calculated the MSDs using the time window method and performed an ensemble average over it, as given by:

$$\langle \overline{\mathbf{s}(t) \cdot \mathbf{s}(t)} \rangle = \frac{1}{N} \frac{1}{T-t} \sum_{i=1}^N \sum_{t'=0}^{T-t} (\mathbf{x}^i(t'+t) - \mathbf{x}^i(t'))^2. \quad (9)$$

In the above equation, the index  $i$  represents an ensemble copy, and  $\mathbf{x}^i(t')$  denotes the position of the center of mass of the flagellar apparatus at time  $t'$  in ensemble copy  $i$ . Here,  $N$  is the total number of ensemble copies, and  $T$  is the total simulation time.

The MSDs of  $FA$  and  $FA_0$  are plotted as a function of time in Fig. 12. For comparison, the MSD of  $FA_{i0}$  is also included. The MSD curve of  $FA$  exhibits a growth of approximately  $\sim t^2$ , indicating ballistic motion up to around 250 beat periods. Beyond this point, the MSD transitions into a diffusive regime with  $MSD \sim t$ . This crossover occurs as the orientation of  $FA$  changes due to rotational diffusion.

The MSD curve of  $FA_{i0}$  follows a  $\sim t$  behavior after an initial transient of approximately ten beats, as expected for thermal diffusion. Similarly, the MSD of  $FA_0$  also tends to  $\sim t$  after the initial transient, indicating that the system is unable to swim and instead undergoes pure diffusion driven by thermal fluctuations. Furthermore, we do not observe any enhancement in the diffusion coefficient of  $FA_0$  compared to that of  $FA_{i0}$  due to its beating activity. This finding aligns with the results in Ref.<sup>74</sup>, which states that diffusion enhancement occurs only in the regime where  $\omega\tau_R \sim 1$ , whereas the current study corresponds to  $\omega\tau_R \gg 1$ . Here,  $\omega = 2\pi/T_b$  represents the angular frequency of flagellar beating, and  $\tau_R$  is the relaxation time for rotational diffusion, which we discuss in the next section.

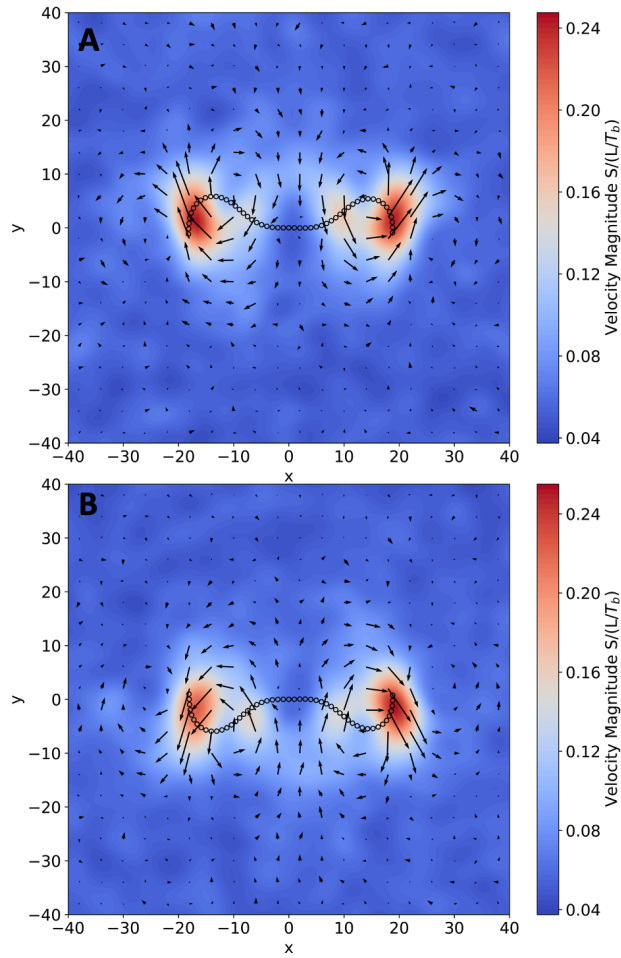


**Figure 9.** Flow fields around the mirror-symmetric phases 3 (A) and 8 (B) of  $FA_0$ . Since the phases themselves are mirror-symmetric, their corresponding flow fields exhibit the same symmetry. Consequently, the displacement induced by phase 3 is canceled by that of phase 8.

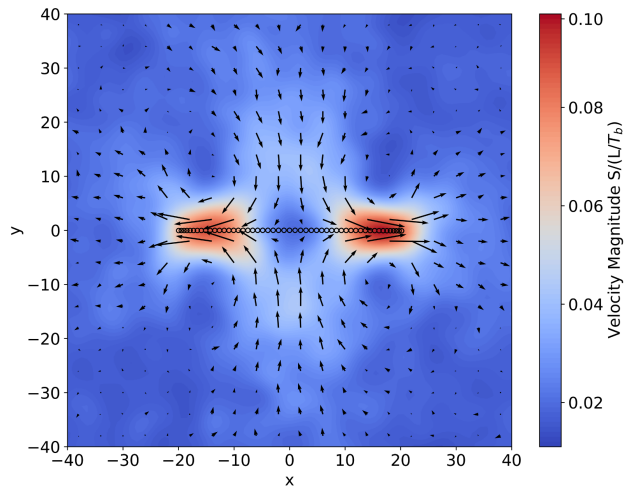


**Figure 10.** Average flow field over a beat of  $FA_0$ . The flow field is symmetric about both the  $x$ - and  $y$ -axes. In the region  $x > 0$ , the flow field resembles that of a flagellum moving to the left, while in the region  $x < 0$ , it resembles that of a flagellum moving to the right.

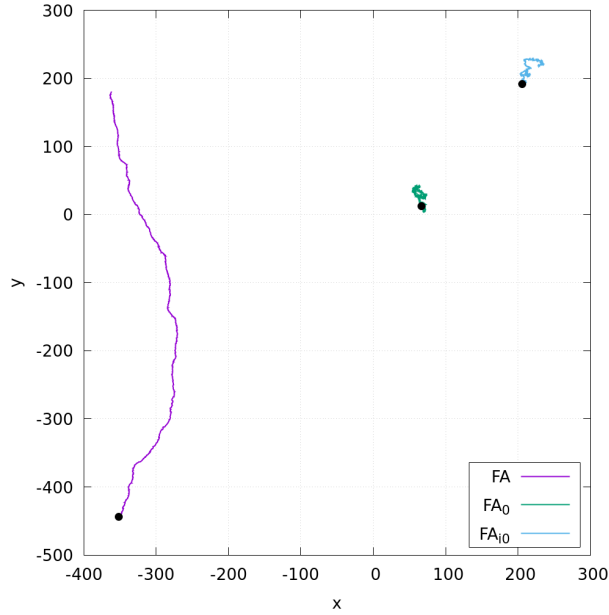


**Figure 11.** Trajectories of  $FA$ ,  $FA_0$ , and  $FA_{i0}$  from MPCD simulations over a period of  $200T_b$ . Both  $FA_0$  and  $FA_{i0}$  exhibit diffusive motion, while  $FA$  moves ballistically until its orientation changes due to rotational diffusion; see Videos 1-3

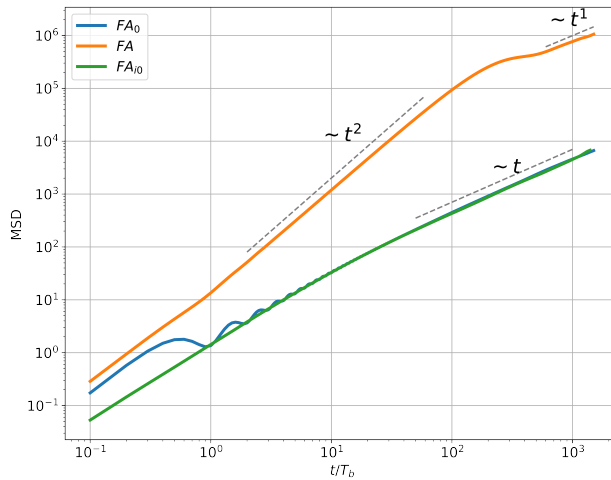


**Figure 12.** Mean square displacements of  $FA$ ,  $FA_0$ , and  $FA_{i0}$  obtained from the hybrid MPCD simulations. Here,  $T_b$  represents the beating period. The  $FA$  exhibits ballistic motion up to approximately 240 beat periods, after which it transitions into a diffusive regime due to rotational diffusion. In contrast,  $FA_0$ , after an initial transient phase, smoothly transitions into diffusion. The MSD curves of  $FA_0$  and  $FA_{i0}$  overlap, indicating that  $FA_0$  does not exhibit active swimming, thereby confirming the validity of the scallop theorem in the presence of fluctuations.

### 4.3.1 Ergodicity

Non-ergodicity introduces randomness into time-averaged quantities, causing them to deviate from their corresponding ensemble averages. Therefore, it is essential to examine the ergodicity of the process to determine whether time averaging yields reliable results.

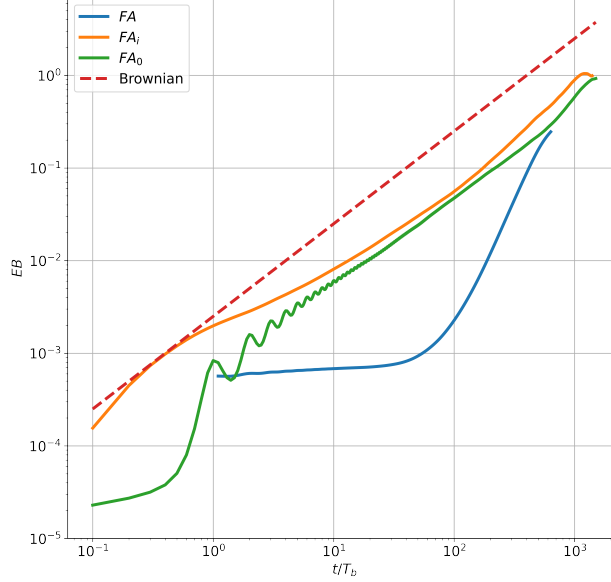


**Figure 13.** Ergodicity breaking (EB) parameter as a function of time lag for  $FA$ ,  $FA_0$ ,  $FA_i$ , and the approximate limit for Brownian motion. All the curves remaining below the Brownian limit indicate that the system is ergodic.

To quantify ergodicity breaking, Burov et al.<sup>75</sup> defined the ergodicity breaking (EB) parameter as:

$$EB(t, T) = \frac{\left\langle \left( \overline{\mathbf{s}(t, T) \cdot \mathbf{s}(t, T)} \right)^2 \right\rangle}{\left\langle \mathbf{s}(t, T) \cdot \mathbf{s}(t, T) \right\rangle^2} - 1, \quad (10)$$

where  $T$  represents the total simulation time. For Brownian motion, in the limit  $t \ll T$ , it has been shown that<sup>76–80</sup>:

$$EB(t, T) \approx \frac{t}{T}. \quad (11)$$

Figure 13 presents the EB parameter as a function of time lag for both active and inactive  $FA$ . The Brownian motion limit of  $EB$  is also shown for reference. Clearly, the  $EB$  values for all  $FA$ s remain below the Brownian limit. This indicates that the dynamics of all  $FA$ s can be considered ergodic, meaning that time averages are representative of ensemble averages.

#### 4.4 Orientation auto-correlation function

We observed a crossover in the MSD curve of  $FA$  from ballistic motion to diffusion (see Fig. 12). This crossover may be attributed to the rotational diffusion of  $FA$ . To quantify the rotational diffusion, we computed the orientation auto-correlation function (OACF). The OACF is determined by first calculating the tangent vector  $\mathbf{e}(t)$  at the center of the flagellar apparatus at each time point. It is then given by  $\langle \mathbf{e}(t') \cdot \mathbf{e}(t' + t) \rangle$ . The OACFs of  $FA$  and  $FA_0$  are shown in Fig. 14. For comparison, we also computed the OACFs of  $FA_i$  and  $FA_{i0}$  and included them in Fig. 14. Interestingly, the OACFs of  $FA$  and  $FA_i$  overlap, and similarly, the OACFs of  $FA_0$  and  $FA_{i0}$  match. This suggests that the beating activity does not significantly affect the rotational diffusion constant of the flagellar apparatus.

The OACFs of both  $FA$  fit well to exponential functions of the form  $e^{-t/\tau_R}$ , as indicated by the dotted lines in Fig. 14. We find that  $\tau_R = 240 T_b$  for  $FA$  and  $\tau_R = 480 T_b$  for  $FA_0$ , both expressed in units of the beat period  $T_b$ . The value of  $\tau_R$  for  $FA$  coincides with the time at which its mean square displacement (MSD) transitions to a diffusive regime, leading us to conclude that this crossover is driven by rotational diffusion. It is important to note that these values of  $\tau_R$  are an order of magnitude smaller than the theoretical calculation, as we discuss below.

Theoretically, we can estimate  $\tau_R$  for a rigid slender cylinder immersed in a fluid with viscosity  $\mu$ . Consider a slender cylinder of length  $L$  and radius  $R$  lying in the  $x$ - $y$  plane. For convenience, we assume that at  $t = 0$ ,

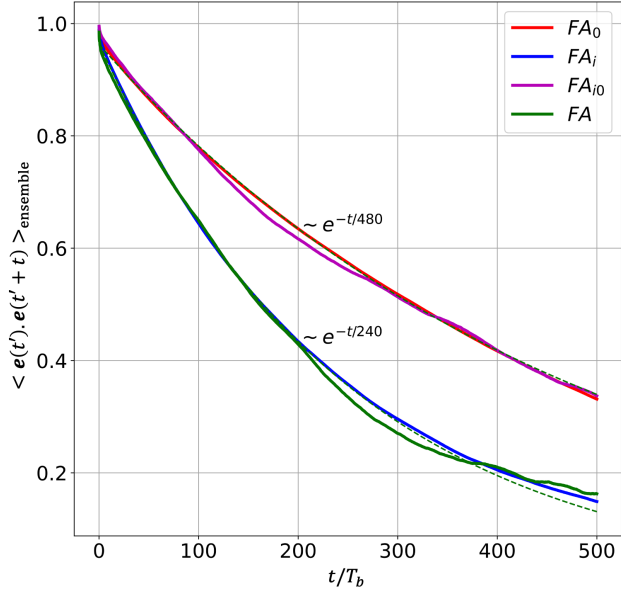


**Figure 14.** Orientation correlation functions of  $FA$ ,  $FA_0$ ,  $FA_i$ , and  $FA_{i0}$ . Dotted lines represent fitted exponential curves of the form  $e^{-t/\tau_R}$ . Slight deviations at the tails of the curves arise due to finite statistical sampling. The overlap of the OACFs of  $FA$  and  $FA_i$ , as well as those of  $FA_0$  and  $FA_{i0}$ , suggests that the beating activity has a negligible effect on rotational diffusion.

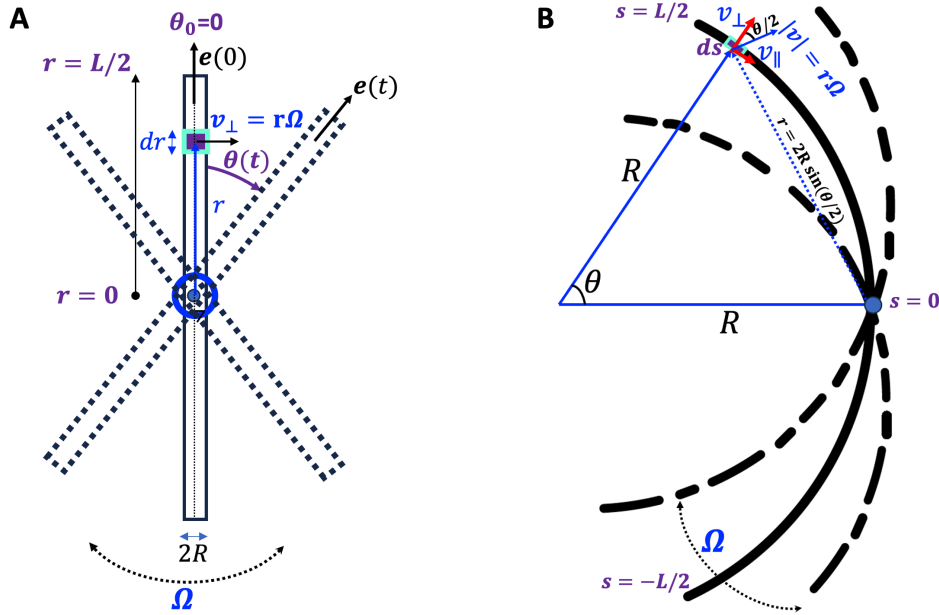


**Figure 15.** (A) A schematic representation of a rigid, slender cylinder of length  $L$  rotating in the  $x$ - $y$  plane about a point passing through its center. (B) A bent, slender cylinder with mean curvature  $C_0 = 1/R$  rotating about its center, marked by a small blue circle.

the cylinder is oriented at an angle  $\theta_0 = 0$ , measured from the  $+y$ -axis. The characteristic time scale  $\tau_R$  for this rigid rod to lose its orientation is related to the rotational diffusion constant  $D_R$  as:

$$\sigma_\theta^2 = \langle (\theta(t) - \theta_0)^2 \rangle = \langle \theta(t)^2 \rangle = 2D_R t. \quad (12)$$

Next, we examine the correlation of the direction vector:

$$\langle \mathbf{e}(t) \cdot \mathbf{e}(0) \rangle = \langle \cos(\theta - \theta_0) \rangle = \langle \cos(\theta) \rangle = \int_{-\infty}^{+\infty} e^{i\theta} p(\theta) d\theta, \quad (13)$$

where  $p(\theta)$  follows a normal distribution:

$$p(\theta) = \frac{1}{\sqrt{2\pi\sigma_\theta^2}} e^{-\frac{\theta^2}{2\sigma_\theta^2}}. \quad (14)$$

Evaluating the integral, we obtain:

$$\langle \cos \theta \rangle = e^{-D_R t}. \quad (15)$$

This result indicates that  $\tau_R = 1/D_R$  represents the time required for the correlation to drop by a factor of  $1/e$ . To relate  $D_R$  to the transverse drag coefficient  $\eta_\perp$  of the cylinder, we consider a scenario where the cylinder rotates at instantaneous angular velocity  $\Omega$  about an axis perpendicular to the  $x$ - $y$  plane (along the  $z$ -direction), passing through its center (see Fig. 15A). The drag torque  $\Gamma_D$  acting on the cylinder is proportional to the angular velocity  $\Omega$ , with the rotational drag coefficient  $\kappa_D$ . We express  $\kappa_D$  in terms of the transverse drag coefficient  $\eta_\perp$  by calculating  $\Gamma_D$  as:

$$\begin{aligned} \Gamma_D^{\text{straight}} &= 2 \int_0^{L/2} d\Gamma_D = 2 \int_0^{L/2} r(f_\perp dr) = -2 \int_0^{L/2} r(\eta_\perp v_\perp) dr \\ &= -2 \int_0^{L/2} r(\eta_\perp r\Omega) dr = -2\eta_\perp \Omega \int_0^{L/2} r^2 dr \\ &= -\frac{1}{12} L^3 \eta_\perp \Omega \approx -0.08 L^3 \eta_\perp \Omega \end{aligned} \quad (16)$$

which gives  $\kappa_D = L^3 \eta_\perp / 12$ . Note that in the equation above,  $f_\perp$  represents the drag force per unit length,  $v_\perp = r\Omega$  is the instantaneous normal velocity of a small radial segment  $dr$ , and the transverse drag coefficient is given by  $\eta_\perp = \frac{4\pi\mu}{\ln(L/R)-0.5}$ <sup>15</sup>. Using Einstein-Smoluchowski relation we obtain:

$$D_R = \tau_R^{-1} = \frac{k_B T}{\kappa_D} = \frac{12k_B T}{L^3 \eta_\perp}. \quad (17)$$

Here, the dynamic viscosity  $\mu$  is given by  $\mu = \nu\rho$ , where the kinematic viscosity  $\nu$  is the sum of two contributions, the kinetic viscosity  $\nu_{\text{kin}}$  and the collision viscosity  $\nu_{\text{col}}$ . It is measured in units of  $a_0^2/\tau_{\text{MPCD}}$  and, with our chosen parameters, equals to  $1.45$ <sup>63</sup>.  $\rho$  is the average particle number in each box, given by  $10m_f/a^2$ .

Next, we repeat the calculation for a slender cylinder of length  $L$  with mean curvature  $C_0 = 1/R$ , where  $R$  is the radius of curvature (see Fig. 15B):

$$\begin{aligned} \Gamma_D^{\text{bent}} &= 2 \int_0^{L/2} \mathbf{r} \times \mathbf{f} ds = 2 \int_0^{L/2} r \frac{\mathbf{f} \cdot \mathbf{v}}{|\mathbf{v}|} ds = -2 \int_0^{L/2} r \frac{\eta_\parallel v_\parallel^2 + \eta_\perp v_\perp^2}{|\mathbf{v}|} ds \\ &= -2R\eta_\perp \int_0^{\frac{L}{2R}} r d\theta \frac{0.5r^2\Omega^2 \sin^2(\frac{\theta}{2}) + r^2\Omega^2 \cos^2(\frac{\theta}{2})}{r\Omega} \\ &= -4R^3\Omega\eta_\perp \int_0^{\frac{L}{2R}} d\theta \sin^2(\frac{\theta}{2}) \left(1 + \cos^2(\frac{\theta}{2})\right) \\ &= -\frac{4}{125} L^3 \Omega \eta_\perp \int_0^{\frac{5}{2}} d\theta \sin^2(\frac{\theta}{2}) \left(1 + \cos^2(\frac{\theta}{2})\right) \\ &\approx -0.04 L^3 \eta_\perp \Omega. \end{aligned} \quad (18)$$

Here,  $\mathbf{f} = -\eta_\perp v_\perp \mathbf{e}_\perp - \eta_\parallel v_\parallel \mathbf{e}_\parallel$  and  $\mathbf{v} = v_\perp \mathbf{e}_\perp + v_\parallel \mathbf{e}_\parallel$ , where  $\mathbf{f}$  is the drag force per unit length, and  $v_\perp$  and  $v_\parallel$  denote the perpendicular and tangential velocity components of the segment  $ds$ , respectively. We take

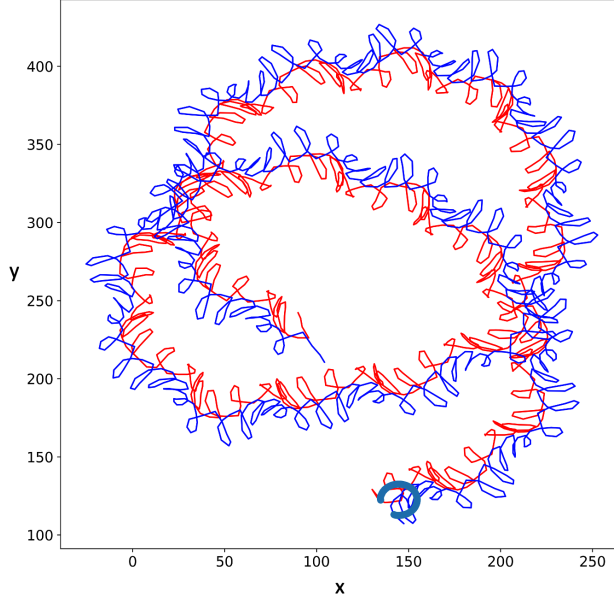


**Figure 16.** Trajectory of the endpoints of an *FA* with arms beating at frequencies  $f_1 = 1/120$  and  $f_2 = 1.2f_1$  (in units of  $\tau_{\text{MPCD}}^{-1}$ ). The arm with the higher frequency traces the inner helix. The *FA* is depicted at the initial instant for visual reference. Due to diffusion, the center of the helix shifts over time. The shape of the *FA* at the final time point is also shown; see also Video 4.

$\eta_{\parallel} = \eta_{\perp}/2$ <sup>15,81</sup> and  $C_0 = 5L^{-1}$ , which is the value used in our simulations. For simplicity, we have ignored the correction to  $\eta_{\perp}$  arising from the mean curvature of the cylinder.

Using the MPCD parameters, we find that  $\tau_D$  for a bent cylinder with mean curvature  $C_0 = 5L^{-1}$  is approximately half of the value for a straight cylinder, which is consistent with our simulation results (see Fig. 14). However, the theoretical estimates are an order of magnitude larger than those obtained from simulations. We attribute this discrepancy to the fact that the finite thickness of the *FA* is completely neglected in the current MPCD model, where the two flagella are represented by connected beads of zero physical size. Experimentally, the radius of a flagellum is approximately 100 nm, which corresponds to about 1% of the length of each flagellum. In our MPCD simulations, the length of a single flagellum was taken as  $25a$  (where  $a$  is the lattice size). To address this discrepancy, we believe that future MPCD simulations should incorporate beads of finite diameter of at least  $a/2$ <sup>82</sup>.

## 5 Flagellar apparatus with asymmetric frequencies

It has been observed in Ref.<sup>55</sup> that most isolated flagellar apparatuses exhibit different frequencies in their arms, with the frequency difference between the arms of an *FA* typically ranging between 10% – 20%. As a consequence of this frequency difference, the *FA* swims along an approximately helical trajectory. To determine whether the current model of *FA* can replicate these experimental observations, we performed simulations of the *FA* with a 20% frequency difference between its arms while keeping all other parameters identical to those described in Section III. We found that under these conditions, the *FA* did not exhibit a helical trajectory. We suspected that the stiffness of the *FA* might be insufficient to sustain helical motion. To test this hypothesis, we conducted additional simulations with higher values of the bending rigidity  $\kappa$  (which was initially set to 200, as prescribed in Ref.<sup>26</sup>). We observed that the bending constant needed to be increased to as high as  $10^4$  in order to reproduce the experimentally observed helical trajectory. The trajectory obtained from simulations using  $\kappa = 10^4$  is shown in Fig. 16. It can be seen that the center of the helix is shifting over time due to diffusion. Thus, we conclude that a single set of MPCD parameters may not be sufficient to reproduce all physical phenomena of the system, and that the parameters must be judiciously chosen depending on the specific behavior being modeled.



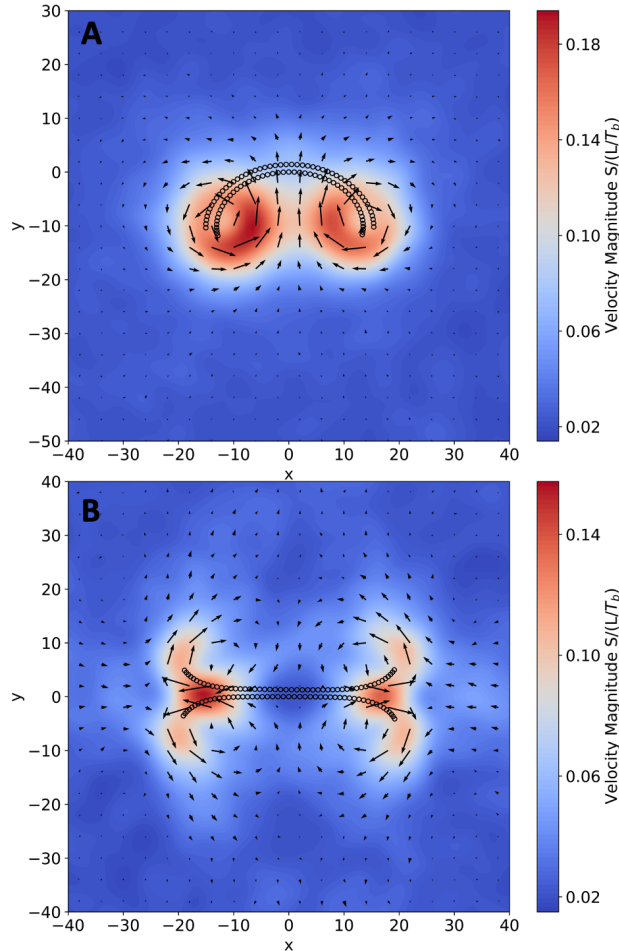


**Figure 17.** Beat-averaged flow field of a pair of *FAs* moving (A) in the same direction and (B) in opposite directions. The flow field in (A) closely resembles that of a single *FA*, with a slight increase in field strength; see Videos 5 and 6.

## 6 Interaction between two *FAs*

Microswimmers are known to form swarms and exhibit collective motion, facilitating efficient navigation through highly viscous fluids<sup>81,83,84</sup>. Hydrodynamic interactions play a crucial role in the emergence of such collective behavior. In this context, we conducted simulations of two *FAs* and analyzed their interactions. Interestingly, we observed that the two *FAs* exhibit mutual attraction and form pairs in two distinct ways.

One form of attraction arises when both *FAs* swim in close proximity along the same axis and in the same direction. In this case, both *FAs* become perfectly aligned along their axis of motion and continue moving together after forming a pair. We found that the average speed over a beat cycle in this configuration is  $0.12 L/T_b$ , which is slightly higher than that of a single *FA*. The flow field averaged over a beat cycle is shown in Fig. 17. The flow field closely resembles that of a single *FA*, which is expected.

The second type of interaction occurs when two *FAs* swim in close proximity but in opposite directions along the same axis. In this case, the *FAs* experience mutual attraction, accompanied by a reduction in the mean curvature of each flagellum. However, their opposing motions cancel out, resulting in no net displacement. Consequently, the *FA* pair undergoes pure diffusion in the fluid. The flow field averaged over a beat cycle is shown in Fig. 17. The absence of swimming may be attributed to the symmetric flow field generated by the pair. The opposing flows along the axis of motion, produced by each *FA*, cancel out at the center, while the flows along the edges remain symmetric and directed in opposite directions. Interestingly, the flow field in Fig. 17 is not entirely similar to that of  $FA_0$ , despite both configurations lacking net propulsion. In contrast to  $FA_0$ , the flow field along the  $x$ -axis is directed toward the *FA* pair. Along the  $y$ -axis, the flow is inward near the *FA* pair but reverses direction at greater distances, pointing outward.

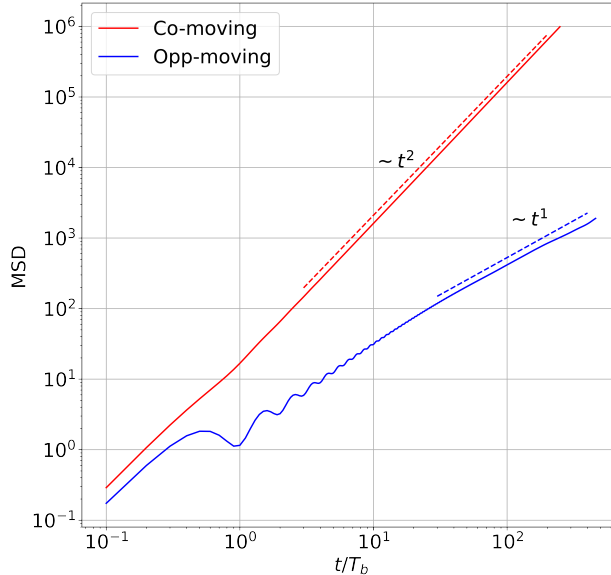


**Figure 18.** MSD of pair of *FAs* moving in same direction and in opposite direction. The co-moving pair moves ballistically at higher speed than *FA* while the pair formed by oppositely moving *FAs* just diffuses.

The MSDs calculated for both cases are shown in Fig. 18. As expected, the co-moving pair exhibits ballistic motion ( $\text{MSD} \sim t^2$ ), while the opposing pair undergoes pure diffusion ( $\text{MSD} \sim t$ ).

## 7 Summary

We modeled the flagellar apparatus (*FA*) of *C. reinhardtii* using multiparticle collision dynamics (MPCD), extending the framework established in Ref.<sup>26</sup>. The *FA* is represented as a string of beads connected by springs, characterized by both spring and bending constants. Propulsion is achieved by imposing sinusoidal traveling waves on the curvature of the system. These waves originate at the center of the *FA* and propagate in opposite directions, mimicking the natural undulations of the *FA*. Using this model, we studied the swimming dynamics and hydrodynamic interactions of the system.

Our simulations reveal that the *FA* swims successfully when modeled with a nonzero average curvature. We determined the speed distributions of various phases and their flow fields, concluding that the *FA* swims as a puller. Analysis of the mean square displacement (MSD) indicated that the *FA* exhibits ballistic swimming for a few hundred beats before transitioning to a diffusion-dominated regime due to rotational diffusion, as the relaxation time for rotational diffusion coincides with the time at which the crossover occurs.

Simulations of an *FA* with zero average curvature ( $FA_0$ ) shows that although the overall shape deformation of the two flagella is non-reciprocal and breaks time symmetry, breaking time symmetry alone is a necessary but not sufficient condition for net propulsion. The  $FA_0$  exhibited negligible random propulsion, with any minor displacement attributed to diffusion induced by thermal fluctuations. This was further validated as its MSD asymptotically matched that of an inactive  $FA_{i0}$ . Furthermore, no significant enhancement in the diffusion coefficient of  $FA_0$  was observed, consistent with the findings of Ref.<sup>74</sup>, which attribute this to the high beating frequency relative to the rotational diffusion relaxation time.

We determined the orientation correlation functions (OACFs) from the simulations and found that the OACFs of *FA* and  $FA_0$  decay exponentially and match their inactive counterparts. This indicates that the beating activity does not influence rotational diffusion. We also simulated the dynamics of an asymmetric *FA*, where the arms beat at different frequencies. To reproduce the experimentally observed helical trajectory, we had to increase the bending constant in the Hamiltonian of the *FA* by several orders of magnitude. This suggests that while the hybrid MPCD method provides promising results, careful tuning of the parameters is necessary to capture the correct physical behavior.

Finally, we investigated the hydrodynamic interactions between two *FAs*. We found that two *FAs* moving along the same axis exhibit mutual attraction regardless of their relative orientations. When two *FAs* move in

---

the same direction, they form a pair that swims together at an increased speed. Conversely, when two *FAs* move head-on, they block each other's motion, resulting in no net movement apart from diffusion.

There are several directions in which this work can be expanded. First, it is crucial to investigate how swimming speed and orientation correlation depend on key MPCD parameters, such as bending rigidity and the spring constant. Second, the role of hydrodynamic interactions should be explored when the two arms of the flagellar apparatus differ in phase, length, and mean curvature. Additionally, experimental observations show a V-shaped junction between the two flagella, where the angle can change over time. Future MPCD simulations should incorporate this junction by introducing a different spring constant for the connecting springs and a potential that allows the angle to vary around a preferred value. Moreover, the finite thickness of the flagella should be included in upcoming MPCD simulations. Lastly, examining the collective motion of multiple flagellar apparatuses and their cluster formation dynamics would yield deeper insights.

In summary, we developed a computational model for the isolated flagellar apparatus of *C. reinhardtii* and investigated its swimming dynamics and hydrodynamic interactions. These findings enhance our understanding of puller-type microswimmers and may provide valuable insights for the design and development of artificial microswimmers.

## Author Contributions

S.V.R. and A.G. contributed equally to the conceptualization, problem formulation, and analysis of the results. S.V.R. performed the coding and simulations. S.V.R. drafted the initial manuscript, and both authors contributed to the revisions.

## Conflicts of interest

“There are no conflicts to declare”.

## Data availability

The data supporting this article have been included as part of the Supplementary Information.

## Acknowledgements

The authors acknowledge insightful discussions with Professors A. Bae and A. Pimir. We are also grateful to Dr. M. Y. Khan for his valuable support during the initial phase of this project. Lastly, we extend our thanks to the High Performance Computing Center at NYUAD for providing the computational resources and data storage for this work.

## Notes and references

1. Y. Yang, J. Elgeti and G. Gompper, *Physical review E*, 2008, **78**, 061903.
2. I. Gibbons, *The Journal of cell biology*, 1981, **91**, 107s–124s.
3. W. Gilpin, M. S. Bull and M. Prakash, *Nature Reviews Physics*, 2020, **2**, 74–88.
4. E. M. Purcell, Physics and our world: reissue of the proceedings of a symposium in honor of Victor F Weisskopf, 2014, pp. 47–67.
5. J. Blake, *Computational Modeling in Biological Fluid Dynamics*, 2001, pp. 1–51.
6. E. Lauga and T. R. Powers, *Reports on progress in physics*, 2009, **72**, 096601.
7. J. Elgeti, R. G. Winkler and G. Gompper, *Reports on progress in physics*, 2015, **78**, 056601.
8. J. Elgeti, U. B. Kaupp and G. Gompper, *Biophysical journal*, 2010, **99**, 1018–1026.
9. N. Taketoshi, T. Omori and T. Ishikawa, *Physics of Fluids*, 2020, **32**, 101901.
10. J. Liu, Y. Fu, Y. Wu and H. Ruan, *Bioinspiration & Biomimetics*, 2024, **19**, 056008.

- 
11. R. Dreyfus, J. Baudry, M. L. Roper, M. Fermigier, H. A. Stone and J. Bibette, *Nature*, 2005, **437**, 862–865.
  12. A. C. Tsang, E. Demir, Y. Ding and O. S. Pak, *Advanced Intelligent Systems*, 2020, **2**, 1900137.
  13. R. Ahmad, A. J. Bae, Y.-J. Su, S. G. Pozveh, E. Bodenschatz, A. Pumir and A. Gholami, *Soft Matter*, 2022, **18**, 4767–4777.
  14. A. J. Bae, R. Ahmad, E. Bodenschatz, A. Pumir and A. Gholami, *PLoS one*, 2023, **18**, e0279940.
  15. J. Gray and G. J. Hancock, *Journal of Experimental Biology*, 1955, **32**, 802–814.
  16. L. J. Fauci and R. Dillon, *Annu. Rev. Fluid Mech.*, 2006, **38**, 371–394.
  17. A. Hilfinger, A. K. Chattopadhyay and F. Jülicher, *Physical Review E—Statistical, Nonlinear, and Soft Matter Physics*, 2009, **79**, 051918.
  18. P. Sartori, V. F. Geyer, J. Howard and F. Jülicher, *Physical Review E*, 2016, **94**, 042426.
  19. S. Camalet, F. Jülicher and J. Prost, *Physical review letters*, 1999, **82**, 1590.
  20. C. J. Brokaw, *Mathematical methods in the applied sciences*, 2001, **24**, 1351–1365.
  21. I. H. Riedel-Kruse, A. Hilfinger, J. Howard and F. Jülicher, *HFSP journal*, 2007, **1**, 192–208.
  22. A. Vilfan and F. Jülicher, *Physical review letters*, 2006, **96**, 058102.
  23. D. J. Hickey, R. Golestanian and A. Vilfan, *Proceedings of the National Academy of Sciences*, 2023, **120**, e2307279120.
  24. Z. Cheng, A. Vilfan, Y. Wang, R. Golestanian and F. Meng, *Journal of the Royal Society Interface*, 2024, **21**, 20240221.
  25. D. Hickey, A. Vilfan and R. Golestanian, *Elife*, 2021, **10**, e66322.
  26. Y. Yang, V. Marceau and G. Gompper, *Physical Review E*, 2010, **82**, 031904.
  27. J. Singleton, E. Diller, T. Andersen, S. Regnier and M. Sitti, 2011 IEEE/RSJ International Conference on Intelligent Robots and Systems, 2011, pp. 1687–1692.
  28. Z. Ye, S. Régnier and M. Sitti, *IEEE Transactions on Robotics*, 2013, **30**, 3–13.
  29. E. Lauga, *Physical Review E—Statistical, Nonlinear, and Soft Matter Physics*, 2007, **75**, 041916.
  30. S. Hu and F. Meng, *Physical Review Letters*, 2024, **132**, 204002.
  31. H. C. Berg, *E. coli in Motion*, Springer, 2004.
  32. C. Brennen and H. Winet, *Annual Review of Fluid Mechanics*, 1977, **9**, 339–398.
  33. T. Omori, H. Ito and T. Ishikawa, *Proceedings of the National Academy of Sciences*, 2020, **117**, 30201–30207.
  34. N. Osterman and A. Vilfan, *Proceedings of the National Academy of Sciences*, 2011, **108**, 15727–15732.
  35. R. E. Goldstein, *Annual review of fluid mechanics*, 2015, **47**, 343–375.
  36. K. Y. Wan and R. E. Goldstein, *Proceedings of the National Academy of Sciences*, 2016, **113**, E2784–E2793.
  37. F. Kendelbacher and H. Stark, *Engineering Of Chemical Complexity*, World Scientific, 2013, pp. 299–319.
  38. C. Wollin and H. Stark, *The European Physical Journal E*, 2011, **34**, 1–10.
  39. W. Liao and E. Lauga, *Physical Review E*, 2021, **103**, 042419.

- 
40. E. H. Harris, *Annual review of plant biology*, 2001, **52**, 363–406.
  41. K. Drescher, R. E. Goldstein, N. Michel, M. Polin and I. Tuval, *Physical Review Letters*, 2010, **105**, 168101.
  42. M. Polin, I. Tuval, K. Drescher, J. P. Gollub and R. E. Goldstein, *Science*, 2009, **325**, 487–490.
  43. R. E. Goldstein, M. Polin and I. Tuval, *Physical review letters*, 2009, **103**, 168103.
  44. K. C. Leptos, K. Y. Wan, M. Polin, I. Tuval, A. I. Pesci and R. E. Goldstein, *Physical review letters*, 2013, **111**, 158101.
  45. N. Uchida and R. Golestanian, *Physical Review Letters*, 2011, **106**, 058104.
  46. R. Golestanian, J. M. Yeomans and N. Uchida, *Soft Matter*, 2011, **7**, 3074–3082.
  47. G. Quaranta, M.-E. Aubin-Tam and D. Tam, *Physical review letters*, 2015, **115**, 238101.
  48. D. L. Ringo, *The Journal of cell biology*, 1967, **33**, 543–571.
  49. M. Melkonian, R. A. Andersen, E. Schnepf, P. Beech, K. Heimann and M. Melkonian, *The Cytoskeleton of Flagellate and Ciliate Protists*, 1991, 23–37.
  50. V. F. Geyer, F. Jülicher, J. Howard and B. M. Friedrich, *Proceedings of the National Academy of Sciences*, 2013, **110**, 18058–18063.
  51. B. M. Friedrich and F. Jülicher, *Physical Review Letters*, 2012, **109**, 138102.
  52. K. Y. Wan and R. E. Goldstein, *Physical review letters*, 2014, **113**, 238103.
  53. M. Sleigh, *Nature*, 1979, **277**, 263–264.
  54. J. S. Hyams and G. G. Borisy, *Science*, 1975, **189**, 891–893.
  55. S. G. Pozveh, A. J. Bae and A. Gholami, *Soft matter*, 2021, **17**, 1601–1613.
  56. J. S. Hyams and G. G. Borisy, *Journal of Cell Science*, 1978, **33**, 235–253.
  57. V. Geyer, *PhD Thesis*, 2013.
  58. D. T. Chen, M. Heymann, S. Fraden, D. Nicastro and Z. Dogic, *Biophysical journal*, 2015, **109**, 2562–2573.
  59. R. Ahmad, C. Kleineberg, V. Nasirimarekani, Y.-J. Su, S. Goli Pozveh, A. Bae, K. Sundmacher, E. Bodenschatz, I. Guido, T. Vidakovic-Koch *et al.*, *ACS synthetic biology*, 2021, **10**, 1490–1504.
  60. A. Gholami, R. Ahmad, A. Bae, A. Pimir and E. Bodenschatz, *New Journal of Physics*, 2022, **24**, 053025.
  61. A. Malevanets and R. Kapral, *The Journal of chemical physics*, 1999, **110**, 8605–8613.
  62. K. Mussawisade, M. Ripoll, R. Winkler and G. Gompper, *The Journal of chemical physics*, 2005, **123**, 144905.
  63. G. Gompper, T. Ihle, D. Kroll and R. Winkler, *Advanced computer simulation approaches for soft matter sciences III*, 2009, 1–87.
  64. M. Y. Khan and S. B. Babu, *Physics of Fluids*, 2022, **34**, 061901.
  65. S. B. Babu and H. Stark, *New Journal of Physics*, 2012, **14**, 085012.
  66. J. L. Münch, D. Alizadehrad, S. B. Babu and H. Stark, *Soft matter*, 2016, **12**, 7350–7363.
  67. A. W. Zantop and H. Stark, *The Journal of Chemical Physics*, 2021, **154**, 024105.

- 
68. S. Mandal and M. G. Mazza, *Physical Review E*, 2019, **99**, 063319.
  69. F. J. Schwarzendahl and M. G. Mazza, *The Journal of Chemical Physics*, 2019, **150**, 184902.
  70. T. Ihle and D. Kroll, *Physical Review E*, 2001, **63**, 020201.
  71. T. Ihle and D. M. Kroll, *Physical Review E*, 2003, **67**, 066705.
  72. Y. Yang, *PhD thesis*, Universität zu Köln, 2009.
  73. G. S. Klindt and B. M. Friedrich, *Physical Review E*, 2015, **92**, 063019.
  74. E. Lauga, *Physical review letters*, 2011, **106**, 178101.
  75. S. Burov, J.-H. Jeon, R. Metzler and E. Barkai, *Physical Chemistry Chemical Physics*, 2011, **13**, 1800–1812.
  76. R. Metzler, J.-H. Jeon, A. G. Cherstvy and E. Barkai, *Physical Chemistry Chemical Physics*, 2014, **16**, 24128–24164.
  77. W. Deng and E. Barkai, *Physical Review E*, 2009, **79**, 011112.
  78. H. Safdari, A. G. Cherstvy, A. V. Chechkin, F. Thiel, I. M. Sokolov and R. Metzler, *Journal of Physics A: Mathematical and Theoretical*, 2015, **48**, 375002.
  79. M. Schwarzl, A. Godec and R. Metzler, *Scientific reports*, 2017, **7**, 3878.
  80. A. G. Cherstvy, S. Thapa, Y. Mardoukhi, A. V. Chechkin and R. Metzler, *Physical Review E*, 2018, **98**, 022134.
  81. J. Gray and H. W. Lissmann, *Journal of Experimental Biology*, 1964, **41**, 135–154.
  82. I. O. Götzke and G. Gompper, *Physical Review E—Statistical, Nonlinear, and Soft Matter Physics*, 2010, **82**, 041921.
  83. H. Moore, K. Dvoráková, N. Jenkins and W. Breed, *Nature*, 2002, **418**, 174–177.
  84. S. Immler, H. D. Moore, W. G. Breed and T. R. Birkhead, *PLoS one*, 2007, **2**, e170.